IEEE Access
Multidisciplinary | Rapid Review | Open Access Journal

Received October 17, 2018, accepted December 20, 2018, date of publication January 1, 2019, date of current version January 29, 2019.

Digital Object Identifier 10.1109/ACCESS.2018.2890458

Spectrum Reconstruction of the Light-Field Multimodal Imager

LIJUAN SU, YUJIAN LIU, AND YAN YUAN

Key Laboratory of Precision Opto-Mechatronics Technology, Ministry of Education, School of Instrumentation and Optoelectronics Engineering, Beihang University, Beijing 100191, China

Corresponding author: Yan Yuan (yuanyan@buaa.edu.cn)

This work was supported by the National Natural Science Foundation of China under Grant 61635002, and also supported in part by the Natural Science Foundation of Beijing Municipality under Grant 4172038 and the Fundamental Research Funds for the Central Universities.

ABSTRACT The multimodal light-field imager can simultaneously capture spectral and polarization characteristic of a two-dimensional target. Due to the diffraction and misalignments of the imaging system, the pixels receive the light passing through different spectral filters and polarizing filters. As a result, the spectral and polarization images constructed by extracting the corresponding filter-pixels contain unwanted information from the other channels. In this paper, we present an imaging model of the spectral and polarimetric radiance for the multimodal light-field imager. Based on the radiance imaging model, calibration schemes are also proposed for determining the spectral response coefficients and polarization response coefficients of the imager. A data reconstruction method based on Tikhonov regularization is proposed to reconstruct the target spectrum with better accuracy. Calibrating and imaging experiments of a prototype are performed and the results confirm the effectiveness of the data reconstruction approach.

INDEX TERMS Multimodal light-field imager, hyperspectral imaging, modeling, calibration, data processing.

I. INTRODUCTION

The hyperspectral and polarimetric imaging systems, which can obtain the intensity, wavelength and polarimetric information, have been used in the earth observation and remote sensing [1]–[3]. The conventional imaging systems rely on the scanning processes to acquire the multi-dimensional (spatial, spectral, polarimetric) information of targets. However, the scanning components and procedures increase the complexity of the systems and introduce motion artifacts to the acquired data. In the past decade, the snapshot multidimensional imagers (SMI) have emerged as a result of the advancements of large format 2D focal plane arrays, high-precision fabrication techniques and the computational techniques [4]. Recently, a light-field architecture has been modified for detecting the spectral and polarimetric information in a single frame [5].

The light-field imaging cameras [6], [7] have been created to capture 2D spatial and 2D angular information of light rays on a 2D plane in a single frame. It has been used for digital refocusing [6], microscope imaging [8], atmospheric turbulence detection [9], depth estimation [10], [11] and multispectral imaging [5], [12]. In 2009, Horstmeyer *et al.* [5] proposed a multimodal imaging system based on a pinhole light-field camera to capture the spectrum, polarization state, and intensity of targets simultaneously. They implemented a filter array of spectral and polarizing filters in the pupil plane of the fore-optics. Each pinhole created a sub-image of the filters array on the sensor, and each filter corresponded to a region of pixels which was called filter-pixel. The sub-image resembles the spectral, polarization and intensity information of the target. In Horstmeyer's design, ''each filter-pixel is typically 5×5 sensor pixels from which a 2×2 or 3×3 block of pixels is sampled and averaged to create synthetic photo pixel''. In this case, the information aliasing among different channels can be neglected. However, there is a tradeoff between the number of filters and the size the of filter-pixel. When the number of pixels covered by a sub-image are fixed, larger size of the filter pixels will lead to smaller number of filtering channels.

In order to increase the number of spectral and polarizing channels, we designed a prototype of which the filter-width corresponding to only one sensor pixel size. We also separated the filters with a width corresponding to a sensor pixel size to reduce the information aliasing among different

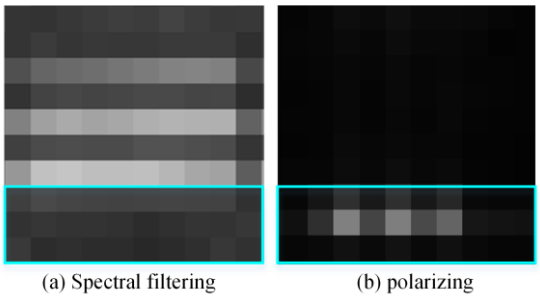

FIGURE 1. A sub-image of white light (a) image with only spectral filters; b) image with only polarizing filters.

channels. However, the pixels still receive multiplexed information from different channels. As shown in Fig.1, the pixels in the area marked by blue lines was designed to receive polarized radiance, whereas the pixels in this area received light passing through both spectral filters and polarizing filters.

In this case, the averaging method used by Horstmeyer cannot restore accurate spectral information obtained by our system. Meng *et al.* [13] proposed a demultiplexing approach to reconstruct the spectrum a four-bandpass multispectral imager. However, the information capturing and reconstruction model of a multimodal imager that captures both spectral and polarimetric information have not been analyzed thoroughly.

In this research, we present the models of spectral imaging and polarization imaging to form the multimodal information acquisition model of the multimodal light-field imager. The spectral calibration scheme is proposed to calibrate the spectral response coefficients based on the spectral imaging model. And the polarization calibration method is also introduced. The data reconstruction algorithm based on regularization is presented to improve the accuracy of the restored spectrum. The spectral coefficients and polarization coefficients of a prototype imager are calibrated based on the proposed calibrating schemes. The restored spectra of different light sources confirm the effectiveness and robustness of the regularization algorithm. Furthermore, the proposed method is used to reconstruct the spectral datacube of a multimodal light filed image.

II. RADIANCE IMAGE MODEL

We begin with a brief introduction of the architecture of our prototype light-field multimodal imager.

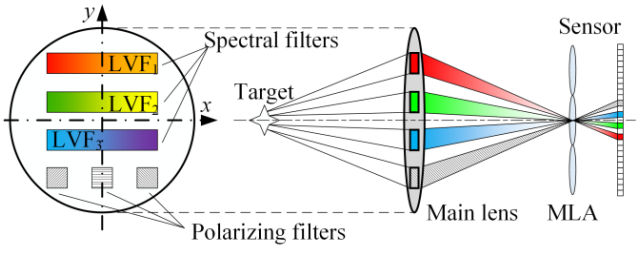

FIGURE 2. Schematic layout of a prototype multimodal light-field imager.

As shown in Fig. 2, the imaging system is simplified into a main lens, a spectral-polarzation-filter-array (SPFA), and a microlens array (MLA) coupled with a sensor. The number of pixels covered by a microlens is H. The filter array consists of several linear variable filters (LVF) and three polarization filters with different polarization angles.

The main lens images a target on a microlens. The light rays originating from this target enter in the pupil of the main lens and pass through different filters. The microlens redirects the filtered light rays on the sensor and formed a sub-images. As a result, the spectrum and polarimetric information of the target is captured at the sensor in a single shot. The sensor converts the radiance L originating from the target to a digital output signal.

A. SPECTRUM IMAGING MODEL

First, we consider imager only with the LVFs to discuss the imaging model of the spectral radiance. Each microlens images an LVF on the sensor to cover several pixels, as shown in Fig. 3. Even though we designed the width of the LVF to conjugate with the width of a pixel, the LVF is imaged on two rows of pixels due to diffraction and misalignment of imaging system.

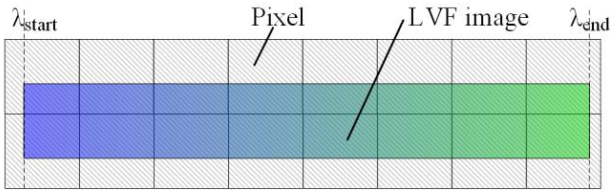

FIGURE 3. Illustration of an LVF image on the sensor.

Considering an arbitrary wavelength λ, the transmittance of the LVF varies along with the length [14], as illustrated in Fig.4. The gray scale indicates the transmittance of the given wavelength. This means the effective aperture of system is not a circle or square aperture as that of normal system.

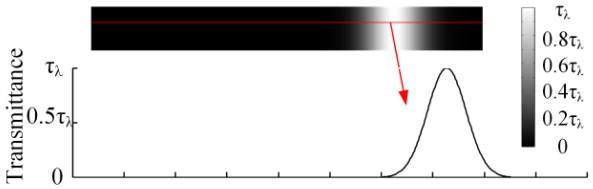

FIGURE 4. Illustration the transmission windows of a mono-spectral wavelength λ.

We note the transmittance of wavelength λ at the position (x, y) on the filter-plane as $\tau_\lambda(x, y)$. Then, the light passing through the filter is given by:

$$\iint_{\mathrm{IA}} \tau_\lambda(x, y)\, L(\lambda) dxdy = \Gamma(\lambda)\, L(\lambda) \tag{1}$$

where, $L(\lambda)$ is spectral radiance of the target, IA is the integrating area of the LVF, and $\Gamma(\lambda)$ is defined as

$$\Gamma(\lambda) = \iint_{\mathrm{IA}} \tau_\lambda(x, y) dxdy \tag{2}$$

The single wavelength light passing through the LVF is received by the several pixels covered by the microlens. And, the j^{th} pixel receives the fraction $\alpha_j(\lambda)$ of the light at wavelength λ. When the wavelength changes, the spectral filtering windows also vary along the length direction as shown in Fig.4. As a result, j^{th} pixel will receive light from a continuous spectral range. This is confirmed by the experimentally measured spectral response curve of a single pixel of the prototype system, as shown in Fig.5.

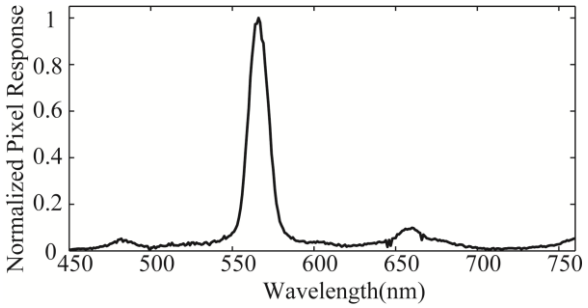

FIGURE 5. The spectral response of a single pixel of a prototype multimodal light-field imager.

Therefore, the digital number (DN) of the j^{th} pixel corresponding to the target spectrum is given by:

$$D_{j,\mathrm{Spec}} = \cos^4\theta \int_{\lambda\mathrm{start}}^{\lambda\mathrm{end}} \frac{\alpha_j(\lambda)\,\Gamma(\lambda)\,L(\lambda)}{r^2} \tau_{\mathrm{o}} \frac{A_{\mathrm{d}} \lambda t}{hc} \rho_j(\lambda) \cdot g_{\mathrm{e}} d\lambda \tag{3}$$

where, θ is the field angle of the target, $[\lambda_{\mathrm{start}}, \lambda_{\mathrm{end}}]$ is the spectral range of the imager, r is the distance between main lens and the microlens, τ_{o} is the transmittance of the optics excluding the spectral filters, A_{d} is the pixel area, $\rho_j(\lambda)$ is the spectral quantum efficiency of the pixel, t is the exposure time, h is the Planck's constant, c is the speed of light, and g_{e} is sensor gain. The discrete version of (3) is given by:

$$D_{j,\mathrm{Spec}} = t \sum_{n=1}^{N} k_{j,n}^S L(\lambda_n) \tag{4}$$

$$k_{j,n}^S = \cos^4(\theta) \frac{\tau_{\mathrm{o}} A_{\mathrm{d}} g_{\mathrm{e}}}{r^2 hc} \lambda \alpha_j(\lambda_n)\,\Gamma(\lambda_n)\,\rho_j(\lambda_n)\,\Delta\lambda \tag{5}$$

If the $\Delta\lambda$ was very small, such as 1 nm, the DNs of all the pixels covered by an arbitrary microlens could be written as in a matrix form as following:

$$\begin{bmatrix} D_1 \\ \vdots \\ D_j \\ \vdots \\ D_H \end{bmatrix}_{\mathrm{Spec}} = t \cdot \begin{bmatrix} k_{1,1}^S & \cdots & k_{1,n}^S & \cdots & k_{1,N}^S \\ \vdots & \vdots & \vdots & \vdots & \vdots \\ k_{j,1}^S & \cdots & k_{j,n}^S & \cdots & k_{j,n}^S \\ \vdots & \vdots & \vdots & \vdots & \vdots \\ k_{H,1}^S & \cdots & k_{H,n}^S & \cdots & k_{H,N}^S \end{bmatrix} \cdot \begin{bmatrix} L_{\lambda_1} \\ \vdots \\ L_{\lambda_n} \\ \vdots \\ L_{\lambda_N} \end{bmatrix} \tag{6}$$

where, $N = 1 + (\lambda_{\mathrm{N}}\text{-}\lambda_1)/\Delta\lambda$. Based on this equation, we could reconstruct the spectral information of target as $\mathbf{L} = [L_{\lambda 1}, \ldots, L_{\lambda n}, \ldots, L_{\lambda N}]^{\mathrm{T}}$ by calibrating the coefficient $k_{j,n}^S$. It requires at least N pixels to sample the spectral range without their spectral response curve totally overlapping with each other. However, in the case of our prototype system, the number of effective sampling pixels is smaller than N.

Assuming the effective spectral channels of the imager is M, the actually measured target radiance is $\overline{\mathbf{L}} = [\overline{L}_1, \cdots, \overline{L}_m, \cdots, \overline{L}_M]$. Here, $\overline{L}_m$ is the average radiance of channel m, and given by:

$$\overline{L}_m = \frac{1}{\lambda_{m,2} - \lambda_{m,1}} \int_{\lambda m,1}^{\lambda \mathrm{m},2} L_m(\lambda) d\lambda \tag{7}$$

where, $[\lambda_{m,1}, \lambda_{m,2}]$ is the spectral range of spectral channel m, and $\lambda_{m,1} = \lambda_{m-1,1} + \Delta\lambda$. In a small range of spectrum, the radiance $L_m(\lambda)$ is normally assumed to be approximately equal $\overline{L}_m$, then the DN contribution of this channel to the j^{th} pixel is can be written as:

$$d_{j,m}^S \approx t \cdot \left(\sum_{n=m,1}^{m,2} k_{j,n}^S \right) \cdot \overline{L}_m = t K_{j,m}^S \overline{L}_m \tag{8}$$

where, coefficients $K_{j,m}^S$ is given by:

$$K_{j,m}^S = \sum_{n=m,1}^{m,2} k_{j,n}^S \tag{9}$$

Then, the digital number of the j^{th} pixel is given as:

$$D_{j,\mathrm{Spec}} = \sum_{m=1}^{M} d_{j,m}^S = \sum_{m=1}^{M} K_{j,m}^S \overline{L}_m \tag{10}$$

And the pixel responses of the spectrum can be written as following equation:

$$\begin{aligned} \begin{bmatrix} D_1 \\ \vdots \\ D_j \\ \vdots \\ D_H \end{bmatrix}_{\mathrm{Spec}} &= t \cdot \begin{bmatrix} K_{1,1}^S & \cdots & K_{1,m}^S & \cdots & k_{1,M}^S \\ \vdots & \ddots & \vdots & \ddots & \vdots \\ K_{j,1}^S & \cdots & K_{j,m}^S & \cdots & k_{j,M}^S \\ \vdots & \ddots & \vdots & \ddots & \vdots \\ K_{H,1}^S & \cdots & K_{H,m}^S & \cdots & k_{H,M}^S \end{bmatrix} \cdot \begin{bmatrix} \overline{L}_1 \\ \vdots \\ \overline{L}_m \\ \vdots \\ \overline{L}_M \end{bmatrix} \\ &= t \cdot \mathbf{K}^S \cdot \mathbf{L} \end{aligned} \tag{11}$$

Here, the coefficient $K_{j,m}^S$ should be nonnegative and its unit is $\mathrm{J}^{-1} \cdot \mathrm{m}^3$, and M is the number of the effective spectral channels.

B. POLARIZATION IMAGING MODEL

For the light-field imager only coupled with polarizing filters, the responses of pixels can be derived similarly as previous section. The radiance passing through the w^{th} ($w = 1, \ldots, W$) linear polarizer is noted as $L_{\mathrm{P}w}(\lambda)$. Since the linear polarizer are bandpass spectral filters, the j^{th} pixel receives

the same portion $K_{j,w}^{P}$ of the radiance at all wavelength. Therefore, the DN of the j^{th} pixel corresponding to the polarimetric information of target is given by:

$$\begin{aligned} D_{j,Pw} &= \cos^4\theta \int_{\lambda\text{start}}^{\lambda\text{end}} \frac{\tau_{Pw}(\lambda)\, K_{j,w}^{P} A_{Pw} L_{Pw}(\lambda)}{r^2} \tau_o \frac{A_d \lambda t}{hc} \rho_j(\lambda) \\ &\quad \cdot g_e d\lambda \\ &= K_{j,l}^{P} D'_{Pw} \end{aligned} \tag{12}$$

where, $\tau_{Pw}(\lambda)$ and A_{Pw} are the transmittance and the area of the w^{th} polarizer respectively. And, D'_{Pw} is given as:

$$D'_{Pw} = \cos^4\theta \int_{\lambda\text{start}}^{\lambda\text{end}} \frac{A_{Pw} L_{Pw}(\lambda)}{r^2} \tau_o \frac{A_d \lambda t}{hc} \rho_j(\lambda) \cdot g_e d\lambda \tag{13}$$

Here, D'_{Pw} can be considered as the DN value of a pixel that receives all the light passing through the w^{th} polarizer. It is determined by the polarized radiance $L_{Pw}(\lambda)$ of the target. Therefore, we use D'_{Pw} to represent the polarization radiance at a selected polarization angle of the target directly. Then, the DNs induced by the polarimetric information are given as following:

$$\begin{aligned} \begin{bmatrix} D_1 \\ \vdots \\ D_j \\ \vdots \\ D_H \end{bmatrix}_{\text{Polar}} &= \begin{bmatrix} K_{1,1}^{P} & \cdots & K_{1,w}^{P} & \cdots & K_{1,W}^{P} \\ \vdots & \ddots & \vdots & \ddots & \vdots \\ K_{j,1}^{P} & \cdots & K_{j,w}^{P} & \cdots & K_{j,W}^{P} \\ \vdots & \ddots & \vdots & \ddots & \vdots \\ K_{H,1}^{P} & \cdots & K_{H,w}^{P} & \cdots & K_{H,W}^{P} \end{bmatrix} \cdot \begin{bmatrix} D'_{P1} \\ \vdots \\ D'_{Pw} \\ \vdots \\ D'_{PW} \end{bmatrix} \\ &= \mathbf{K}^{P} \cdot \mathbf{D}_P \end{aligned} \tag{14}$$

Here, $K_{j,w}^{P}$ is percentage coefficient without unit and should satisfy the following relationship:

$$\sum_{j=1}^{j=H} K_{j,w}^{P} = 1 \quad j = 1, \cdots, H \; K_{j,w}^{P} \geq 0 \tag{15}$$

C. MULTIMODAL INFORMATION IMAGING MODEL

In a multimodal light-field imager used for spectrum and polarization imaging, a pixel may receive radiance passing through spectral filters and polarizing filters due to diffraction and misalignments of the system components. Therefore, the spectral and polarimetric information multiplexing model can be obtained by combining (11) and (14) and given as:

$$\mathbf{D} = \begin{bmatrix} t\mathbf{K}^{S} & \mathbf{K}^{P} \end{bmatrix} \cdot \begin{bmatrix} \mathbf{L} \\ \mathbf{D}_P \end{bmatrix} + \mathbf{N}_{\text{sensor}} = \mathbf{K}\mathbf{X} + \mathbf{N}_{\text{sensor}} \tag{16}$$

where $\mathbf{D} = [D_1, \ldots, D_j, \ldots, D_H]^{\text{T}}$ is the responses of the pixels covered by a microlens, $\mathbf{K}$ is the coefficient matrix which consists of spectral coefficients $\mathbf{K}^{\text{S}}$ and polarization coefficients $\mathbf{K}^{\text{P}}$, $\mathbf{X}$ is determined by the spectrum $\mathbf{L}$ and polarimetric information $\mathbf{D}_{\text{P}}$ of the target. And $\mathbf{N}_{\text{sensor}}$ is the noise vector of observed data due to system noises, which are the readout noise and quantization noise of sensor. This equation relates the sensor response **DN** to the target information $\mathbf{X}$ by a multiplexing matrix $\mathbf{K}$. Once the coefficients $K_{j,m}^{S}$ and $K_{j,w}^{P}$ are determined, the spectrum and polarimetric information of the targets can be obtained by applying the inverse algorithms.

III. SYSTEM CALIBRATION AND DATA RECONSTRUCTION

In order to extract the spectral datacube and polarization images of different angles, the coefficients of matrix $\mathbf{K}$ should be calibrated before applying an algorithm to solve (16). Furthermore, the algorithm should be robust to data errors caused by system noises and calibration errors.

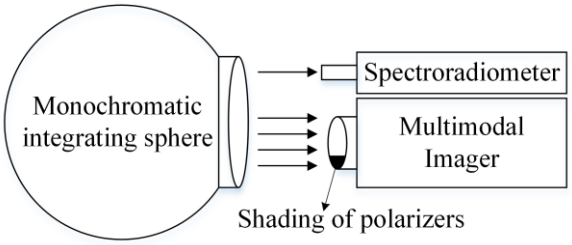

FIGURE 6. Schematic layout of spectral calibration setup for the multimodal light-field imager.

A. CALIBRATION OF SPECTRAL COEFFICIENTS

The schematic setup for obtaining the spectral coefficients is illustrated in Fig.6. A shading is installed in front of the main lens to block the linear polarizers. Therefore, the light only passes through the LVFs during this calibration. The monochromatic integrating sphere generates uniform light that can fulfill the entire field of view of the prototype imager. The central wavelength λ_n of the monochromatic integrating sphere can be changed during the calibration process. A spectroradiometer (ASD Inc.) is introduced to measure the irradiance of the monochromatic light source.

Once the output of the monochromatic integrating sphere is stable, the multimodal imager takes an image and the spectraradiometer record the source irradiance. Then the coefficient $k_{j,n}^{S}$ of an arbitrary microlens can be calculated by following equation:

$$k_{j,n}^{S} = d_j^{S}(\lambda_n) \Big/ t_e L_{\text{Ref.}}(\lambda_n) \tag{17}$$

where, $d_j^{S}(\lambda_n)$ is the DN of the j^{th} pixel recorded at wavelength λ_n, t_e is the exposure time of the imager and $L_{\text{ref.}}(\lambda_n)$ is the irradiance of the light source measured by the spectroradiometer. The entire spectral range of the system is scanned by changing the central wavelength of output light with every $\delta\lambda$ change. Then, we can calculated the coefficient $K_{j,m}^{S}$ by using (9).

B. CALIBRATION OF POLARIZATION COEFFICIENTS

Fig. 7 illustrates the schematic setup for calibrating the polarization coefficients. The LVFs are also blocked by a shading to only allow light passing through polarizers. A linear polarizer is placed in front the panchromatic integrating sphere to generate a linear polarized light with radiance value $L_{P0}(\lambda)$. Based on the Marius' Law, the radiance passing through the w^{th} polarizer in the imager is defined as:

$$L_{Pw}^{C}(\lambda) = L_{P0}(\lambda) \cos^2(\beta + \varphi_{Pw}) + b_w \tag{18}$$

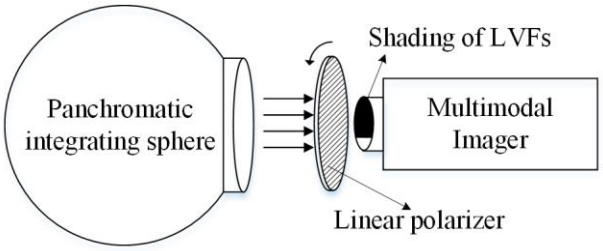

FIGURE 7. Schematic layout of polarization calibration setup for the multimodal light-field imager.

where, β is the transmission axis angle of the rotating polarizer, $\varphi_{\mathrm{P}w}$ is the known transmission axis angle of the w^{th} polarizer, and the offset b_w is due to the imperfect extinction ratio of rotating linear polarizer and the w^{th} linear polarizer.

Combining (18) and (12), the DN of j^{th} pixel correspoding to the light passing through the w^{th} polarizer is given by:

$$d_{j,w}^{P}(\beta) = K_{j,w}^{P}\left[D'_{\mathrm{P}w0}\cos^2(\beta+\varphi_{\mathrm{P}w})+b_w\right] = K_{j,w}^{P} I_{\mathrm{P}w}(\beta) \tag{19}$$

where, $I_{\mathrm{P}w}(\beta) = D'_{\mathrm{P}w0}\cos^2(\beta+\varphi_{\mathrm{P}w})+b_w$, and $D'_{\mathrm{P}w0}$ is given by (13). During the calibration process, the linear polarizer is rotated from 0° to 180° and the imager takes image after every $\Delta\beta = 1°$ change. The recorded image data at any polarization angle should satisfy (14) and can be rewritten as:

$$\begin{bmatrix} D_1(i\Delta\beta) \\ \vdots \\ D_H(i\Delta\beta) \end{bmatrix} = \begin{bmatrix} K_{1,1}^{P} & \cdots & K_{1,W}^{P} \\ \vdots & \ddots & \vdots \\ K_{H,1}^{P} & \cdots & K_{H,W}^{P} \end{bmatrix} \begin{bmatrix} I_{\mathrm{P}1}(i\Delta\beta) \\ \vdots \\ I_{\mathrm{P}W}(i\Delta\beta) \end{bmatrix} \tag{20}$$

where, $i = 1, 2, \ldots, 180$. The polarization coefficients are calculated by a nonlinear least-square fitting algorithm using the cost function given by:

$$\chi^2 = \min\left\{\sum_{i=1}^{180}\widetilde{\mathbf{D}}(i\Delta\beta) - \mathbf{D}(i\Delta\beta)\right\} \tag{21}$$

where, $\widetilde{\mathbf{D}}(i\Delta\beta)$ is the fitted pixel responses, and $\mathbf{D}(i\Delta\beta)$ is the actually measured pixel responses.

C. SPECTRUM RECONSTRUCTION ALGORITHM

Once the coefficients of matrix $\mathbf{K}$ are obtained, we can reconstruct the target spectral and polarizing information by calculating the solution $\mathbf{X}$ of (16). The problem described by (16) is a discrete ill-posed problem. Its solution can be obtained by minimizing $\|\mathbf{KX}\text{-}\mathbf{D}\|$. A most commonly used algorithm is the least squares (LS) algorithm used by Meng [13], which directly taking the pseudoinverse of the calibrated response matrix $\mathbf{K}$. Then, the restored information is given by:

$$\hat{\mathbf{X}}_{\mathrm{LS}} = \left(\mathbf{K}^{\mathrm{T}}\mathbf{K}\right)^{-1}\mathbf{K}^{\mathrm{T}}\mathbf{D} \tag{22}$$

However, the accuracy of the spectrum reconstructed by LS algorithm is sensitive to the errors of coefficient matrix $\mathbf{K}$ and the measured data $\mathbf{D}$. The solution can be less sensitive to perturbations of $\mathbf{K}$ and $\mathbf{D}$ by implementing regularization method. In this research, we use the Tikhonov regularization (TR) method [15] to solve the problem. The Tikhonov regularized solution is defined as the solution to the following least squares problem as the following problem:

$$\underset{\mathbf{n}_1,\mathbf{n}_2}{\operatorname{argmin}}\ \{\|\mathbf{KX}-\mathbf{D}\|^2 + \gamma^2\|\boldsymbol{l}\mathbf{X}\|^2\} \tag{23}$$

where, γ is the regularization parameter that controls the weight given to minimization of the constrain $\|\boldsymbol{l}\mathbf{X}\|$ of the solution relative to the minimization of the residual norm $\|\mathbf{KX}\text{-}\mathbf{D}\|$, and the matrix $\boldsymbol{l}$ acts as a regularization operator. Normally, the matrix $\boldsymbol{l}$ is a discrete derivative operator. However, in the multimodal light-field imager, the polarimetric information of different linear polarizing angles is independent of each other. As a result, the smoothing derivative can only apply to the spectrum part of the solution. Therefore, the matrix $\boldsymbol{l}$ for our problem is given by:

$$l = \begin{bmatrix} \boldsymbol{l}_2 & \mathbf{0} \\ \mathbf{0} & \mathbf{I}_W \end{bmatrix}_{(M+W-2)\times(M+W)} \tag{24}$$

where, $\mathbf{I}_W$ is a $W \times W$ identity matrix for polarization solution part, $\boldsymbol{l}_2$ is a $(\mathrm{M}-2)\times\mathrm{M}$ discrete approximation of the 2nd derivative operator for spectral solution part. The $\boldsymbol{l}_2$ is given by following equation:

$$\boldsymbol{l}_2 = \begin{bmatrix} -1 & 2 & -1 & & \\ & \ddots & \ddots & \ddots & \\ & & -1 & 2 & -1 \end{bmatrix}_{(M-2)\times(M} \tag{25}$$

The solution of (23) is given by:

$$\hat{\mathbf{X}}_{\mathrm{TR}} = (\mathbf{K}^{\mathrm{T}}\mathbf{K} + \gamma^2\boldsymbol{l}^{\mathrm{T}}\boldsymbol{l})^{-1}\mathbf{K}^{\mathrm{T}}\mathbf{D} \tag{26}$$

Therefore, the reconstructed spectrum of the target is given by:

$$\overline{L}_m = \hat{x}_m \quad m = 1, \ldots, M \tag{27}$$

IV. EXPERIMENTAL RESULTS

In this section, we present the experimental results of a prototype multimodal light-field imager. The customized LVFs and polarizing filters are mounted on a circular glass plate. The wavelength range of spectral filters is 450nm - 765nm. And the polarization angles of the polarizing filters are 45°, 90° and 135°. The microlens array, which is produced by the Advanced Microoptic System Gmbh (aμs) of Germany, is placed on the imaging plane of the fore-optics. The size of each microlenes is 55 μm × 55 μm and the focal length is 0.22mm. The Viewworks VA-29MC sensor is coupled at the back focal plane of the mircolens array. The detector pixel size is 5.5 μm × 5.5 μm. Therefore, the sub-image of the prototype covers 10 × 10 pixels.

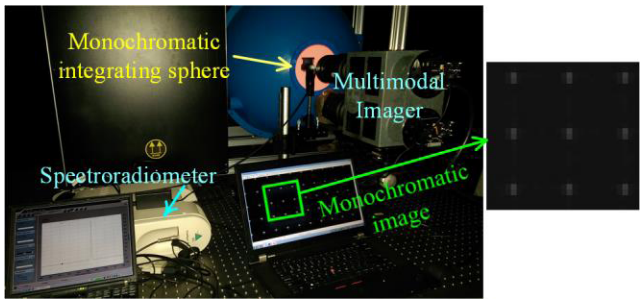

FIGURE 8. The spectral calibration setup for obtaining the monochromatic images.

A. RESULTS OF COEFFICIENTS CALIBRATION EXPERIMENTS

The spectral calibration setup of the prototype multimodal imager has been built and is shown in Fig. 8. The output wavelength of monochromatic integrating sphere is changed for obtaining the spectral response of pixels covered by an arbitrary microlens. The calibration procedures include: 1) take the light field spectral image of the uniform monochromatic output and measure the radiance of the light by the spectroradiometer, 2) scan the spectral range of the system with $\delta\lambda$ every step and repeat step 1), 3) extract intensities of pixels at different wavelength to calculate the spectral coefficients $K^S_{j,m}$ by using (9). The spectral coefficients of an arbitrary sub-image are plotted in the Fig. 9. Here, the 10×10 pixels covered by a microlens are numbered by every ten pixels from the same column.

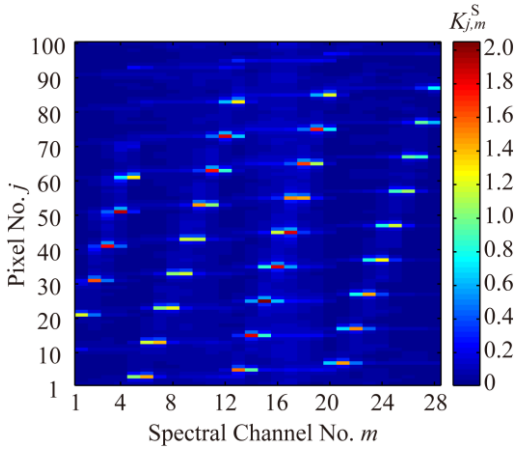

FIGURE 9. The calibrated spectral coefficients of pixels covered by a microlens.

The polarization calibration setup of the prototype imager is shown in Fig.10(a). Fig.10(b) shows sub-images with incident light polarized at different angles. The marked three pixels corresponds to three different polarizing channels of the prototype respectively. By rotating the linear polarizing filter placed in front of the output of the integrating sphere, we can obtain polarization images at different polarization angles and draw the response curves of pixels as illustrated

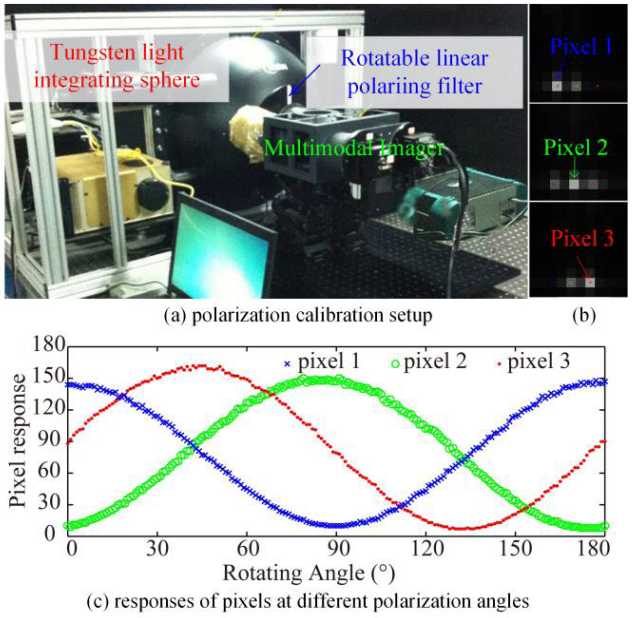

FIGURE 10. The polarization calibration: a) the setup, b) the sub-images at three different polarizing angles, c) the responses of pixels when rotating the polarizing filter.

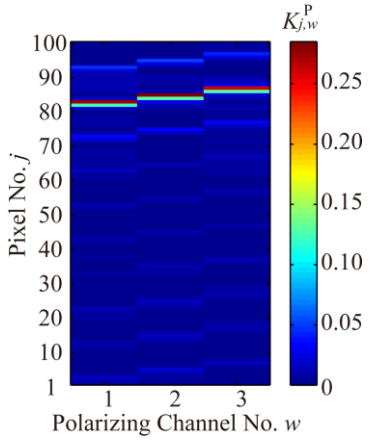

FIGURE 11. The calibrated polarization coefficients of pixels covered by a microlens.

in Fig.10(c). The polarization coefficients can be calculated by using (21) to fit all the polarization response curves of all the pixels. The calculated polarization coefficients of an arbitrary microlens are plotted in Fig. 11.

B. RECONSTRUCTED SPECTRUM

Once the spectral and polarization coefficients are determined, the spectra of targets can be restored from the recorded multimodal light-field images by applying de-multiplexing algorithms. Fig. 12 shows the sub-images behind an arbitrary microlens when the system is illuminated by the tungsten and xenon light sources.

In this research, as discussed in section III-C, the imaged spectral and polarization data of targets are reconstructed

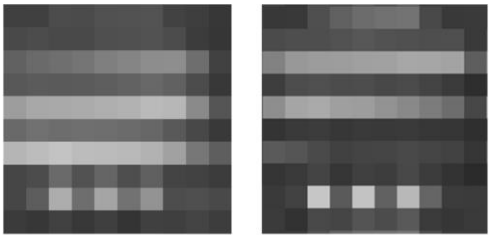

FIGURE 12. The sub-images of different light sources. (a) Tungsten light. (b) Xenon light.

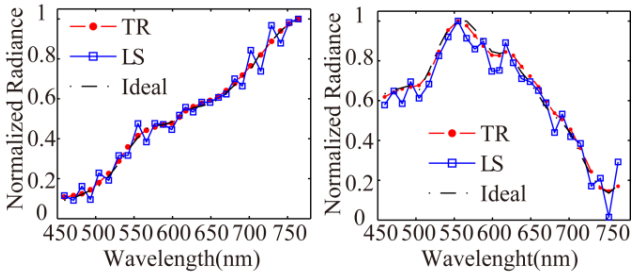

FIGURE 13. The reconstructed spectra of two different light sources. (a) Tungsten light. (b) Xenon light.

by using the LS and TR methods to calculate $\mathbf{X}$ of (16). And the spectra of targets are extracted by using (29). The restored spectra of the tungsten and xenon light sources are shown in Fig.13, in which the 'Ideal' refers to the reference spectra of the light sources measured by the same spectro-radiometer used in the calibration procedure. Comparing the reconstructed spectra, the spectral curves obtained by the TR algorithm are much closer to the reference spectral curves than those reconstructed by the LS algorithms are.

In order to evaluate the performance of the spectral reconstruction algorithms, we use the criterion spectral angle mapper (SAM) [16], which is given as:

$$SAM = \cos^{-1}\left(\frac{\mathbf{L}_R^{\mathrm{T}}\hat{\mathbf{L}}_C}{\|\mathbf{L}_R\|\left\|\hat{\mathbf{L}}_C\right\|}\right) \tag{28}$$

where, $\mathbf{L}_R$ and $\hat{\mathbf{L}}_C$ are the reference spectrum and the calculated spectrum respectively. Here, the *SAM* describes the distortion of the calculated spectrum from the reference spectrum. And, smaller value of *SAM* means that the restored spectrum is more similar to the reference spectrum. The spectra of a 300×300 microlens area were reconstructed by the two algorithms, the average and root-mean-square error (RMS) of *SAM*s of the light source spectra are given by:

$$\overline{SAM} = \sum_{q=1}^{Q} SAM_q \Big/ Q \tag{29}$$

$$\sigma_{SAM} = \sqrt{\sum_{q=1}^{Q} \left(SAM_i - \overline{SAM}\right)^2 \Big/ Q} \tag{30}$$

TABLE 1. The SAMs for different light sources.

	Tungsten		Xenon	
	LS	TR	LS	TR
$SAM_{\min}$	1.82°	0.92°	2.41°	1.41°
$\overline{SAM}$	6.34°	2.15°	6.66°	2.68°
σ_{SAM}	3.76°	0.44°	3.72°	0.39°

where, Q is the total number of sub-images in the selected area. The minimum, average and RMS of the *SAM* of different light sources are summarized in table 1. The smaller values of $SAM_{\min}$ and $\overline{SAM}$ indicate that the TR algorithm can obtain better results than the LS algorithm can. Furthermore, smaller value of σ_{SAM} also shows that the TR algorithm performs with better robustness when the noises are different at different sub-images.

Further imaging experiment was performed to obtain a multimodal light-field image of several buildings, as shown in Fig.14. The sub-images of different building surfaces are enlarged and also illustrated in Fig.14.

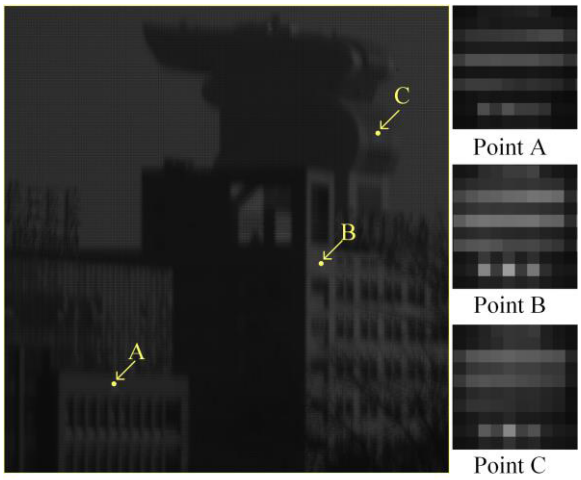

FIGURE 14. The multimodal light-field image of buildings.

FIGURE 15. The spectral datacube and color image of the same scene. (a) Spectral datacube. (b) Color image.

The spectra of the sub-images are extracted by using the TR algorithm to form the spectral datacube of the entire scene. Fig.15(a) shows the datacube image generated by

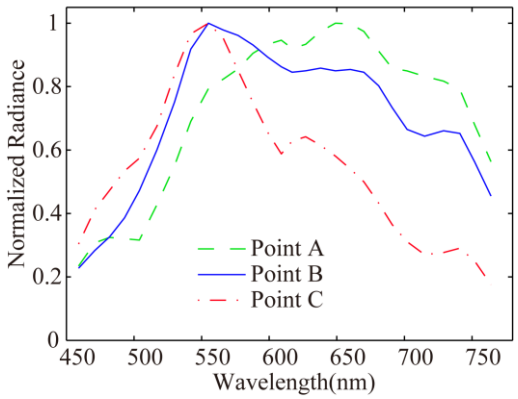

FIGURE 16. The reconstructed spectra of three building surfaces.

the software. We also took a color image the buildings by using a commercial Canon camera. There are slightly color differences between the two images, because the three channels chosen to generate datacube image have spectral ranges that are different from the spectral ranges of the RGB channels of the Canon camera.

The spectra of the three typical surfaces are shown in Fig. 16. The point A is a wall with red color which corresponds to the relatively large radiance in the wavelength range of [600nm, 730nm]. The spectral curve of point C has a peak around wavelength 550nm, and its curve coincides with its green color. For point B, its spectral curve has a peak near 550nm and relatively large radiance from 550nm to 670nm.

V. CONCLUSIONS

In this paper, we present a radiance imaging model to describe the relationships between the target radiance and the sensor responses of a multimodal light-field imager. This model including the spectral radiance imaging model and the polarization radiance imaging model. Based on these two models, calibration schemes are proposed to determine the spectral coefficients and polarization coefficients of the imaging system. In the data reconstruction process, we also introduce the TR algorithm to minimize the reconstruction error introduced by the system noises and calibration errors. The spectral and polarization calibration setups are built to calibrate a prototype of multimodal light-field imager. The spectra of different light sources are reconstructed from the acquired imaged data by two algorithms. The quantitatively results of criterion SAM confirm that the TR approach can restore the spectrum more accurately than the LS algorithm can. The spectral datacube of buildings is also obtained by reconstructing all the light-field sub-images of the captured scene. In summary, the data reconstruction methodology proposed in this paper include an imaging model, two calibration schemes and a de-multiplexing algorithm. And the presented de-multiplexing algorithm can reconstruct the target spectrum with better quality.

REFERENCES

[1] K. Yu and C. Hu, "Changes in vegetative coverage of the Hongze Lake national wetland nature reserve: A decade-long assessment using MODIS medium-resolution data," *J. Appl. Remote Sens.*, vol. 7, p. 073589, Feb. 2003.

[2] A. W. Nolin and J. Dpzoer, "A hyperspectral method for remotely sensing the grain size of snow," *Remote Sens. Environ.*, vol. 74, no. 2, pp. 207–216, Nov. 2000.

[3] F. Snik *et al.*, "An overview of polarimetric sensing techniques and technology with applications to different research fields," *Proc. SPIE, Polarization, Meas., Anal., Remote Sens. XI*, vol. 9099, p. 90990B, May 2014, doi: 10.1117/12.2053245.

[4] L. Gao and L. V. Wang, "A review of snapshot multidimensional optical imaging: Measuring photon tags in parallel," *Phys. Rep.*, vol. 616, pp. 1–37, Feb. 2016.

[5] R. Horstmeyer, G. Euliss, R. Athale, and M. Levoy, "Flexible multimodal camera using a light field architecture," in *Proc. IEEE Int. Conf. Comput. Photogr.*, San Francisco, CA, USA, Apr. 2009, pp. 1–8.

[6] R. Ng, M. Levoy, M. Brédif, G. Duval, M. Horowitz, and P. Hanrahan, "Light field photography with a hand-held plenoptic camera," Stanford Univ., Stanford, CA, USA, Tech Rep. CSTR 2005-02, 2005, pp. 1–11.

[7] T. Georgiev and A. Lumsdaine, "Focused plenoptic camera and rendering," *J. Electron. Imag.*, vol. 19, no. 2, p. 021106, Apr. 2010.

[8] M. Levoy, Z. Zhang, and I. Mcdowall, "Recording and controlling the 4D light field in a microscope using microlens arrays," *J. Microsc.*, vol. 235, pp. 144–162, Apr. 2009.

[9] C. Wu, J. Ko, and C. C. Davis, "Determining the phase and amplitude distortion of a wavefront using a plenoptic sensor," *J. Opt. Soc. Amer. A, Opt. Image Sci.*, vol. 32, no. 5, pp. 964–978, May 2015.

[10] A. Klein, T. Yaron, E. Preter, H. Duadi, and M. Fridman, "Temporal depth imaging," *Optica*, vol. 4, no. 5, pp. 502–506, May 2017.

[11] Y. Chen, X. Jin, and Q. Dai, "Distance measurement based on light field geometry and ray tracing," *Opt. Express*, vol. 25, no. 1, pp. 59–70, Jan. 2017.

[12] L. Su, Z. Zhou, Y. Yuan, Y. Yuan, and S. Zhang, "A snapshot light field imaging spectrometer," *Optik*, vol. 126, pp. 877–881, May 2015.

[13] L. Meng, T. Sun, R. Kosoglow, and K. Berkner, "Evaluation of multispectral plenoptic camera," *Proc. SPIE, Digit. Photography IX*, vol. 8660, p. 86600D, Feb. 2013, doi: 10.1117/12.2006293.

[14] P. J. Murr, B. R. Wiesent, F. Hirth, and A. W. Koch, "Thin film measurement system for moving objects based on a laterally distributed linear variable filter spectrometer," *Rev. Sci. Instrum.*, vol. 83, no. 3, p. 035110, 2012.

[15] G. H. Golub, P. C. Hansen, and D. P. O'Leary, "Tikhonov regularization and total least squares," *SIAM J. Matrix Anal. Appl.*, vol. 21, no. 1, pp. 185–194, Jan. 1997.

[16] S. E. Qian and G. Chen, "Enhancing spatial resolution of hyperspectral imagery using sensor's intrinsic keystone distortion," *IEEE Trans. Geosci. Remote Sens.*, vol. 50, no. 12, pp. 5033–5048, Dec. 2012.

LIJUAN SU received the B.E. degree from the University of Science and Technology of China, Hefei, China, in 2003, the M.E. degree from the Chinese Academy of Sciences, Beijing, China, in 2006, and the Ph.D. degree from The Ohio State University, Columbus, OH, USA, in 2010. She is currently an Associate Professor with Beihang University, Beijing. Her current research interests include imaging spectrometer, light field imaging, and precision metrology.

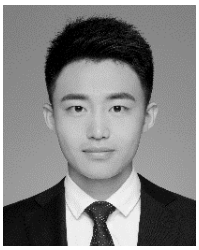

YUJIAN LIU received the B.E. degree from Beihang University, Beijing, China, in 2016, where he is currently pursuing the M.S. degree. His current research interests include polarimetric-spectro imager and data process.

YAN YUAN received the B.E. degree from the University of Science and Technology of China, Hefei, China, in 1990, and the M.E. and Ph.D. degrees from the Xi'an Institute of Optics and Precision Mechanics, The Chinese Academy of Sciences, Xi'an, China, in 1997 and 2005, respectively.

She is currently a Professor with Beihang University, Beijing, China. Her current research interests include spectral imaging technology, optical instrument design, light field photography, and modeling on optical characteristics of space target.